energies

MDPI

Article

Comparison of Zirconium Redistribution in BISON EBR-II Models Using FIPD and IMIS Databases with Experimental Post Irradiation Examination

Kyle M. Paaren *, Spencer Christian, Luca Capriotti, Assel Aitkaliyeva and Douglas Porter

Idaho National Laboratory, 2525 Fremont Ave, Idaho Falls, ID 83415, USA; spencer.christian@inl.gov (S.C.); luca.capriotti@inl.gov (L.C.); aitkaliyeva@mse.ufl.edu (A.A.); douglas.porter@inl.gov (D.P.)
* Correspondence: kyle.paaren@inl.gov

Abstract: Metallic fuels have seen increased interest for future sodium fast reactors due to their material properties: high thermal conductivities and advantageous neutronic properties allow for greater fission densities. One drawback to typical metallic fuels is zirconium redistribution, which impacts this advantageous material and its neutronic properties. Unfortunately, the processes behind zirconium migration behavior are understood using first principles, so before these fuels are implemented in future fast reactors, characterization and fuel qualification regimes must be completed. These activities can be supported through the use of robust modeling using the most accurate empirical models currently available to fuel researchers around the world. The tool that allows researchers to model this complex coupled thermo-mechanical behavior and nuclear properties is BISON. Additionally, BISON model parameters need to be compared against PIE measurements. The current work utilizes two fuel pins from EBR-II experiment X441 to optimize various model parameters, including porosity correction factor, thermal conductivity, phase transition temperature, and diffusion coefficient multipliers, before implementing the final model for seven fuel pins with differing characteristics. To properly evaluate the BISON simulations, the results are compared to PIE metallography data for each fuel pin, to ensure the zirconium redistribution is properly reflected in the simulation results. Six out of seven analyzed fuel pins demonstrate good agreement between the metallography images and BISON results, showing alignment of the Zr-rich, Zr-depleted, and moderately Zr-enriched zones at various axial heights along the fuel pins. Further work is needed to refine the model parameters for general pin use.

Keywords: BISON; simulation; finite element methods; EBR-II; automation; metallic fuel; validation; metallography

Citation: Paaren, K.M.; Christian, S.; Capriotti, L.; Aitkaliyeva, A.; Porter, D. Comparison of Zirconium Redistribution in BISON EBR-II Models Using FIPD and IMIS Databases with Experimental Post Irradiation Examination. *Energies* **2023**, *16*, 6817. https://doi.org/10.3390/en16196817

Academic Editors: Gašper Žerovnik, Alessandro Del Nevo, Pablo Romojaro and Aljaž Čufar

Received: 28 August 2023
Revised: 18 September 2023
Accepted: 19 September 2023
Published: 26 September 2023

1. Introduction

Substantial work has been conducted previously to link the IFR Materials Information System (IMIS) and Fuels Irradiation and Physics Database (FIPD) to BISON input files through automation to show the capability of coupling these databases to a predictive modeling program [1]. However, the previous work in the fuel performance qualification space neglected zirconium (Zr) redistribution due to computational cost and focused on comparing Post Irradiation Examination (PIE) data for the initial validation. Modeling Zr redistribution is important, as zirconium concentration affects peak fuel temperature and material properties within the fuel matrix. This ultimately affects fuel performance metrics and contributes to failure criteria, such as fuel-cladding mechanical interaction (FCMI) and fuel-cladding chemical interaction (FCCI), along with fuel properties. Being able to accurately predict zirconium redistribution within fuel is vital for qualifying a customer's design. The work presented in this manuscript aims to couple zirconium redistribution into the fuel pin models that were previously modeled with automated BISON files linked to IMIS and FIPD. This work was conducted to analyze the effect zirconium redistribution

has on fuel performance by comparing the BISON simulation results against PIE data. The BISON fuel performance code simulation results were compared to recent metallography data for a qualitative analysis of zirconium redistribution modeling [2–7]. Different pin compositions, geometries, and irradiation histories were used to show the validity of modeling zirconium redistribution within BISON.

The reason constituent migration within fuel, such as zirconium redistribution, is so important, is due to prediction of various fuel performance phenomena when licensing new types of fuel and predicting fuel behavior during accidents. In the development of advanced fuel forms, accident-tolerant fuels are being doped and manufactured with different constituents to increase melting temperature, decrease fuel volumetric swelling and creep, and reduce FCMI and FCCI. In the instance of reactor accidents, constituent redistribution may also occur when fuel and cladding melt and fuse together in a total meltdown, as was the case within the Fukushima Daiichi accident. In the case of a complete core meltdown, constituent redistribution within corium is important, as it determines melted fuel behavior.

Previous work with BISON, a fuel performance code developed and maintained at INL, successfully modeled zirconium redistribution at various levels of burnup [2,7,8]. This work included a limited dataset of zirconium redistribution from rods T179, DP11, DP16, and DP 81 irradiated in Experimental Breeder Reactor II (EBR-II) during experiments X419, X441, and X447. These rods range in burnup from 1.9 to 11 at.% burnup [2,3,6]. To properly model these rods, BISON input parameters were specified, including geometric dimensions, coolant inlet temperatures, and coolant mass flowrate [7]. The results of these previous BISON models were compared to Electron probe microanalysis (EPMA) scans and found to be in agreement when using lower diffusion coefficients within the model [7].

The U-Pu-Zr redistribution model was used in previous work to explore the effect both axial power profile shifts and axial variations in the plutonium content have on the radial zirconium redistribution. To see the effect plutonium content had on Zr redistribution, plutonium content was varied linearly from 20 at.% at the bottom end of the rod to 0 at.% at two-thirds of the rod height from the bottom of the rod [8]. This was performed to show the impact on fuel performance for advanced fast reactors. Plutonium content was limited in the top third of the fuel in part of this study due to greater cracking observed in U-Pu-Zr fuels and to limit Fuel Cladding Chemical Interaction (FCCI) [8,9]. Varying the axial power profile as a function of time reproduced the previous axial zirconium redistribution results and temperature profile for the T179 rod out of EBR-II experiment X419 [7,8]. Varying the plutonium content axially from 20 at.% to 0 at.% substantially reduced the amount of gamma phase uranium within the T179 fuel matrix and reduced the maximum fuel temperature by 50 K [8]. Decreasing the plutonium content also showed a significant decrease in radial zirconium redistribution.

In order to confirm the Zr redistribution modeling is completed, a comparison with experimental data is critical. Optical metallography and radial core drilling from EBR-II experiment X423 and SEM, with EDS analysis, from Fast Flux Test Facility (FFTF) experiment MFF-3 were also performed [3,4]. Each of these pins contained fuel compositions of U-xPy-10Zr alloys, with the plutonium content $x \leq 30$ weight percent for experiment X423 [4]. In the case of the FFTF experiment analysis, the plutonium content was zero. The fuel pin sections had burnups ranging from 0.4 to 5.7 at.% [3,4]. A high concentration uranium, low zirconium radial region is seen in both of these studies at ~5 at.% burnup, with the uranium ring starting to form at 1.9 at.% burnup from the pin within experiment X423 [3]. These and other analyses of experiments were previously used to construct redistribution models [8–10].

IMIS and FIPD do not contain SEM images, corresponding Energy Dispersive X-ray Spectroscopy (EDS), nor EPMA data of the pin cross-sections for all EBR-II fuel pins [11,12]. BISON simulations previously performed implemented a power and flux history that follow GLASS power data contained within FIPD, variable flowrates, fabricated dimensions, and phase compositions. Previous work modeling zirconium redistribution did not have as

detailed irradiation conditions available [2,3,6]. Due to the lack of PIE SEM and EPMA data, seven out of the 1977 unique EBR-II metallic fuel pin models were created with the same input parameters as the initial EBR-II models, with zirconium redistribution added to them [1]. Zirconium redistribution was inserted into the BISON simulations to compare axial and radial zirconium redistribution predictions with metallography. Uranium- and zirconium-rich zones from BISON simulations and were compared qualitatively against metallography images. Out of the 1977 fuel pin models developed, only seven pins are presented and examined in depth.

EPMA examination has been performed on various EBR-II and FFTF fuel pins to identify phase transitions and zirconium redistribution within metallic U-Zr and U-Pu-Zr fuels [2–7]. Radial cuts of T179 and DP16 fuel rods were made and imaged using SEM, as well as radial cuts of fuel rod T459 at various axial heights, to illustrate the diffusion process of zirconium within the metallic fuels [2]. EPMA scans from different pins allowed for the diffusion coefficients to be optimized for general use, which is beneficial to comparing metallic fuel pins that ran under different operating conditions and obtained different burnups [2].

The goal of this work is to provide a qualitative analysis of zirconium redistribution modeling within the BISON fuel performance code by comparing simulation results to optical metallography over legacy metallic fuel pins. Out of the seven pins presented, four pins were examined and compared to metallography results recently conducted at Idaho National Laboratory (INL) and three pins were compared to metallography conducted at Argonne National Laboratory (ANL) from 1989 to 1991. The pins included in this study are summarized in Table 1. Each of these pins represent a different final burnup and temperature conditions, which allows for differences to be seen between axial and radial zirconium redistribution. In this contribution, qualitative comparisons between the BISON predicted radial and axial zirconium redistribution zones and metallography scans were made, and differences between the zirconium zones were identified.

Table 1. EBR-II pins examined in BISON.

Pin	Experiment	Fuel Type	Cladding Type	Smear Density (%)	Average Burnup (at. %)
A812	X441/441A	U-19Pu-10Zr	D9	75	10.2
DP20	X441	U-19Pu-10Zr	HT9	75	4.84
DP21	X441/441A	U-19Pu-10Zr	HT9	75	10.1
DP29	X441/441A	U-19Pu-14Zr	HT9	75	11.1
DP45	X441/441A	U-19Pu-10Zr	HT9	85	8.87
DP61	X441/441A	U-19Pu-10Zr	HT9	70	10.7
T653	X430/430A/430B	U-19Pu-10Zr	HT9	75	9.91

2. Methods

2.1. BISON Modeling and Input Parameters

All BISON models used in this work are based on a modified generic EBR-II model to include zirconium redistribution [1,13,14]. IMIS and FIPD provide the geometric dimensions and operating conditions to be written into BISON input files. A total of 1977 unique BISON models were created with current data found within IMIS and FIPD [1]. An overview on the process to construct a generic BISON input file is explained in previous work [1]. This overview includes how the operating conditions and geometric dimensions are parsed and written into each input file, as well as postprocessing of simulation results to compare against PIE data within the databases. Changes to the generic EBR-II BISON input file will be described in this section, in addition to an explanation of how the postprocessing of simulation data changed in order to compare against images produced from metallography. EBR-II fuel pins selected for zirconium redistribution comparisons to metallography images include T653 from experiment X430, DP20 from experiment X441, and DP45 from experiment X441. Additionally, BISON modeling predictions for pins A812, DP21, DP29,

and DP 61 from experiment X441 were compared against metallography. These pins were chosen as they represent different burnups, power histories, and smeared densities.

Previously, EBR-II GLASS power data was parsed to provide an accurate, high resolution power history without increasing computational time significantly. The GLASS data was originally used to detect fission gases in the argon cover gas, but it also contained the EBR-II power history data over the operating lifetime of the reactor. Depending on the way the GLASS data was parsed, the process yielded a minimum number of time steps required to complete a BISON simulation, limiting the time step change to these points. With the addition of zirconium redistribution into the BISON input file, the maximum time step taken within each simulation has to be reduced to accommodate the increased convergence criteria [10]. This increases the minimum number of timesteps within each simulation, increasing the computational time needed. BISON input parameters being parsed will be performed the same way as previous work to isolate the effect that implementing zirconium redistribution has on the simulation results and the comparison to PIE data [1]. For this work, an iterative adaptive method was utilized to increase the time step when convergence occurs and decrease the time step when the problem does not converge; a maximum time step of 50,000 s was allowed.

Los Alamos National Laboratory (LANL) provides documentation pertaining to the modeling of zirconium redistribution within BISON and the coupling of various material models together [10]. Results and recommendations used within the previous work were carried over to the BISON modeling performed in this manuscript. Results were presented to compare Neumann and Dirichlet boundary conditions for zirconium redistribution at the edge of the fuel, with the Dirichlet condition seeing less zirconium at the boundary [9]. For mesh convergence with zirconium redistribution, it was recommended that a minimum of 100 radial elements should be used to obtain accurate results. A limited time step of 1500 s was used to prevent numerical oscillations within the Fission Gas Release postprocessor [10].

The implementation of zirconium redistribution into the BISON input file adds instability within the system and causes spikes in residuals when using the previous coarse mesh [13]. To compensate for the tightly coupled system, the number of elements radially and axially within the fuel were significantly increased. For accurate zirconium redistribution results, it is recommended that a minimum of 80 radial elements are used [10]. This is due to the zirconium concentration solver being mesh-dependent, with a coarse mesh resulting in unphysical negative values in some elements during a power cycle. In order to keep the aspect ratio similar to previous work performed with the generic EBR-II input file, the mesh over the fuel contains 80 radial elements and 100 axial elements. The increase in mesh elements on the fuel allows for fewer instabilities within the system. While the finer mesh is beneficial for convergence, it leads to an increase in the computational time and memory needed to complete the simulation.

Additions to the EBR-II input file include coupling zirconium redistribution with existing material models being used. Zirconium content was defined as solution variable such that the residuals were considered for convergence. Instead of the zirconium content in the U-Pu-Zr fuel matrix defined as a constant in the global parameters block, the initial zirconium content is set as an initial condition in the variables block. This allows for Zr concentration to be solved as a variable. A Neumann boundary condition of zero was applied to the outer fuel surface to mimic previous experimental zirconium redistribution results at the fuel outer radius caused by ZrO_2 powder that is used to insert the fuel matrix into the fuel elements.

Zirconium diffusion is handled by the ZirconiumDiffusion kernel contained within the BISON code. Within the material block, zirconium content was coupled to all applicable material models, except for the burnup material model which requires a constant value. The ZirconiumDiffusion kernel is fed the Fickian and Soret diffusivity properties calculated by the ZrDiffusivityUPuZr material model. The ZrDiffusivityUPuZr model requires diffusion coefficients, diffusion modifiers, and diffusion activation energy multipliers for each phase

of the fuel (alpha, beta, gamma, and delta). BISON default modeling parameter values, based on previous work comparing zirconium redistribution and EPMA data, were utilized for the diffusion modifiers and diffusion activation energies [2]. The diffusion coefficient multipliers used are described in detail below.

Figure 1 shows the coupling of material properties and which phenomena affect fuel behavior. Material model coupling used to describe material properties for the fuel and the cladding are listed in Table 2 with the corresponding BISON object.

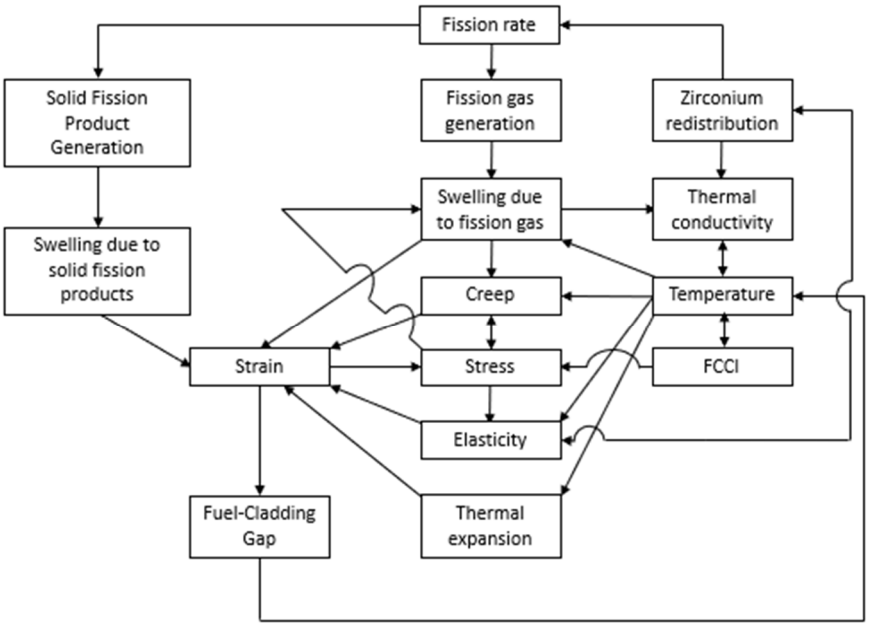

Figure 1. BISON coupled material properties.

Table 2. BISON objects used in BISON simulations.

Phenomenon	Fuel	Cladding
Fuel Phase	PhaseUPuZr [15]	N/A
Thermal Conductivity	UPuZrThermal [16,17]	ThermalD9 [18–20] ThermalHT9 [18,21] Thermal316 [22]
Porosity Correction	UPuZrSodiumLogging [23]	N/A
Density (g·cm^{-3})	15.8	7.8
Burnup	UPuZrBurnup [24]	N/A
Fission Rate	UPuZrFissionRate [25]	N/A
Elasticity Tensor	UPuZrElasticityTensor [18]	D9ElasticityTensor [18] HT9ElasticityTensor [26] SS316ElasticityTensor [26]
Zirconium Redistribution	ZrDiffusivityUPuZr [2,4,15]	N/A
Creep	UPuZrCreepUpdate [18]	D9CreepUpdate [18] HT9CreepUpdate [18] SS316CreepUpdate [27]
Thermal Expansion	UPuZrThermalExpansionEigenstrain [28]	D9ThermalExpansionEigenstrain [18] HT9ThermalExpansionEigenstrain [20] SS316ThermalExpansionEigenstrain [29]
Gaseous Swelling with Hot-Pressing Pore Collapse	UPuZrGaseousEigenstrainwithHotPressingPuswelling [24,30,31]	N/A
Fission Gas Release	UPuZrFissionGasRelease [32]	N/A
Solid Swelling	BurnupDependentEigenstrain [30]	N/A
Cladding Void Swelling	N/A	D9VolumetricSwellingEigenstrain [33] HT9VolumetricSwellingEigenstrain [18] SS316VolumetricSwellingEigenstrain [34]
FCCI	N/A	MetallicFuelWastage [25] MetallicFuelWastageDamage [25]
CDF	N/A	FailureCladHT9 [35] FailureCladD9 [34]

Given the interconnectivity of the various BISON objects and material models, changes in one property, such as the fuel thermal conductivity, can impact the zirconium redistribution throughout the fuel pin. Additionally, recently developed material models—the porosity correction factor models—can alter the required diffusion coefficient multipliers which were previously optimized for general pin use [2]. Even without the updated material models, the previous work conceded that the zirconium zones did not reflect the zones seen in PIE data [2].

To account for the implementation of new material properties and to further optimize various coefficients—the diffusion coefficient multipliers and phase transition temperatures—numerous trial tests were conducted and compared to metallography data. Pins DP45 and DP61 were selected for this initial study due to the difference in smeared density and average burnup. The tested parameter values and coefficients from previous work are summarized in [1,2].

Numerous vector postprocessors were added to the base EBR-II input file, including the output of the radial zirconium redistribution at different axial heights, where the metallography was taken, as well as the centerline zirconium redistribution. This was performed to compare zirconium redistribution with previous work and to compare uranium and zirconium zones with metallography images. Each vector postprocessor was written to a separate csv file, later extracted by Python. A Python postprocessor script was written to compare axial and radial zirconium redistribution with metallography images [1]. Further documentation over models and parameters used in the modified EBR-II input file may be found in the BISON documentation and BISON users' manual [25].

Parameter values contained within Table 3 were simulated to determine those which best reflect the zirconium redistribution zones position and thickness seen in DP45 PIE data [2]. Figure 2 displays the Zr mole fraction contours comparing the fractional porosity correction factor model and the sodium-logged porosity correction factor model. The fractional model results in a thick Zr-rich zone, along the entire axial length of the fuel pin, which extends to approximately half the radius of the pin. The logged porosity model results in less overall Zr migration across the entire axial length. The difference between the two models is especially prevalent near the base of the fuel pin. The Zr-rich zone in the logged porosity model results only slightly touches the bottom of the fuel pin, whereas the Zr-rich zone in the fractional model results covers roughly one-third of the fuel pin bottom. This led to a better comparison with the metallography and removed thermal-stripping artifacts from the simulations, and therefore is recommended to use for this classification of problems.

Table 3. Parameter values.

Phase Transition Temperatures	α-β Transition Temperature		β-γ Transition Temperature	
Default	868.15 K		923.15 K	
Galloway	965.15 K		995.15 K	
D0_scale	Alpha	Beta	Delta	Gamma
Default	1	1	1	1
Galloway	45×10^{-6}	2.28×10^{-5}	3×10^{-6}	3.85×10^{-4}
Kim	15.0	20.0	15.0	20.0

The parameter optimization results from DP45 testing are seen in Table 4; DP45 and DP61 of experiment X441 were chosen to test the various model parameter combinations due to their difference in smeared densities and at.% burnup. Examining the model combinations above, combinations (a), (e), (f), and (j) cause the Zr-rich zone, indicated in red, to migrate farther than the central zone seen in the metallography images. Combinations (b), (c), (g), and (h) only reach a Zr mole fraction of approximately 23%, which does not reach the expected Zr mole fraction of approximately 50% seen in past EPMA data [2]. Combination (d), while similar to (i), reflects the Zr-rich and Zr-depleted zones at the 78%

axial height slightly better than combination (i). Model combination (d) utilized the LANL thermal conductivity model, default diffusion coefficient multipliers, and the elevated phase transition temperatures found in Galloway [2].

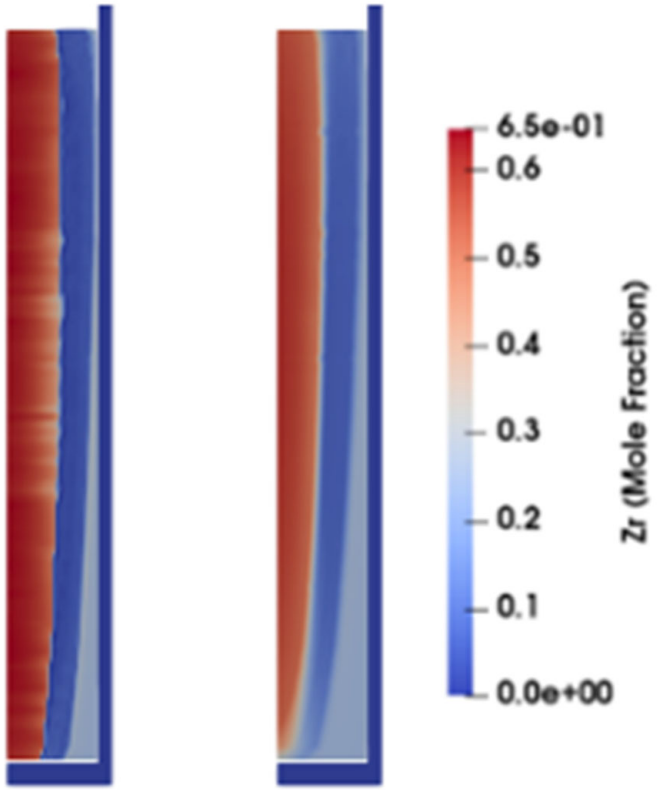

Figure 2. Porosity correction factor model comparison. **Left**: Fractional (default); **right**: logged.

The model combination results from DP61 support the conclusion that combination (d) most accurately reflects the Zr zones. However, the Zr-rich and Zr-depleted zones at the 78% axial height and 89% axial height still migrated farther radially through the fuel pin than seen in metallography. This migration indicated a need to further refine the model parameters or thermal boundary conditions. Adjusting the models from combination (a) to (d), only the phase transition temperatures were modified, from the default values to the Galloway values, causing a reduction in Zr migration and improvement in the simulation of Zr zones. The preliminary optimization of the various modeling parameters used in this work for metallography comparison utilized the LANL thermal conductivity model for U-Pu-Zr fuel with a logged porosity correction factor with phase transition temperatures by Galloway [2].

2.2. Metallography Sectioning

The metallography for four out of the seven pins was utilized for comparison against BISON zirconium redistribution simulation results. The other three pins, DP21, DP29, and DP61, were examined previously by ANL. Of the seven pins that are compared in this study, the cutting diagram for the fuel column in pin T653 from experiment X430B illustrates a representative cutting plan for all the fuel pins. The cutting diagram used for T653 is shown in Figure 3, with the X/L positions for all seven pins listed in Table 4. This sectioning scheme was chosen to investigate the evolution of the microstructure as a function of axial and radial temperature distributions, in addition to the change in axial burnup. The radial and longitudinal cuts were performed to length as specified in Figure 3, mounted in epoxy, and polished to a 0.25 µm finish.

Table 4. DP45 model parameter results. Red within the table signifies a Zr-rich zone, blue being a Zr-depletion zone, and gray being the nominal starting value at the beginning of the simulations.

X/L = 0.78 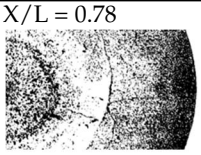 X/L = 0.50 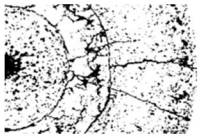	X/L = 0.78 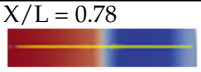 X/L = 0.50 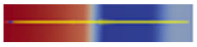	X/L = 0.78 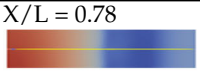 X/L = 0.50 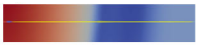	X/L = 0.78 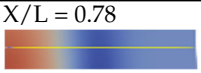 X/L = 0.50 	X/L = 0.78 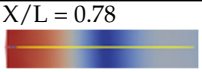 X/L = 0.50 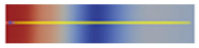	X/L = 0.78 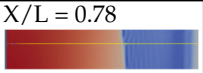 X/L = 0.50 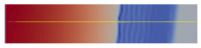
Metallography	TC Model: LANL D0_scale coefficient: Default Phase Transition Temperatures: Default	TC Model: LANL D0_scale coefficient: Galloway Phase Transition Temperatures: Default	TC Model: LANL D0_scale coefficient: Galloway Phase Transition Temperatures: Galloway	TC Model: LANL D0_scale coefficient: Default Phase Transition Temperatures: Galloway	TC Model: LANL D0_scale coefficient: Kim Phase Transition Temperatures: Default
	(a)	**(b)**	**(c)**	**(d)**	**(e)**
X/L = 0.78 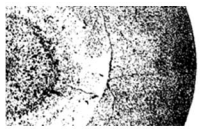 X/L = 0.50 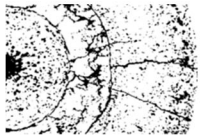	X/L = 0.78 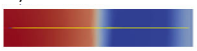 X/L = 0.50 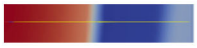	X/L = 0.78 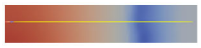 X/L = 0.50 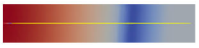	X/L = 0.78  X/L = 0.50 	X/L = 0.78 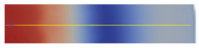 X/L = 0.50 	X/L = 0.78 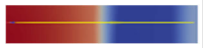 X/L = 0.50 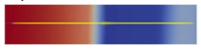
Metallography	TC Model: Galloway D0_scale coefficient: Default Phase Transition Temperatures: Default	TC Model: LANL D0_scale coefficient: Galloway Phase Transition Temperatures: Default	TC Model: LANL D0_scale coefficient: Galloway Phase Transition Temperatures: Galloway	TC Model: LANL D0_scale coefficient: Default Phase Transition Temperatures: Galloway	TC Model: LANL D0_scale coefficient: Kim Phase Transition Temperatures: Default
	(f)	**(g)**	**(h)**	**(i)**	**(j)**

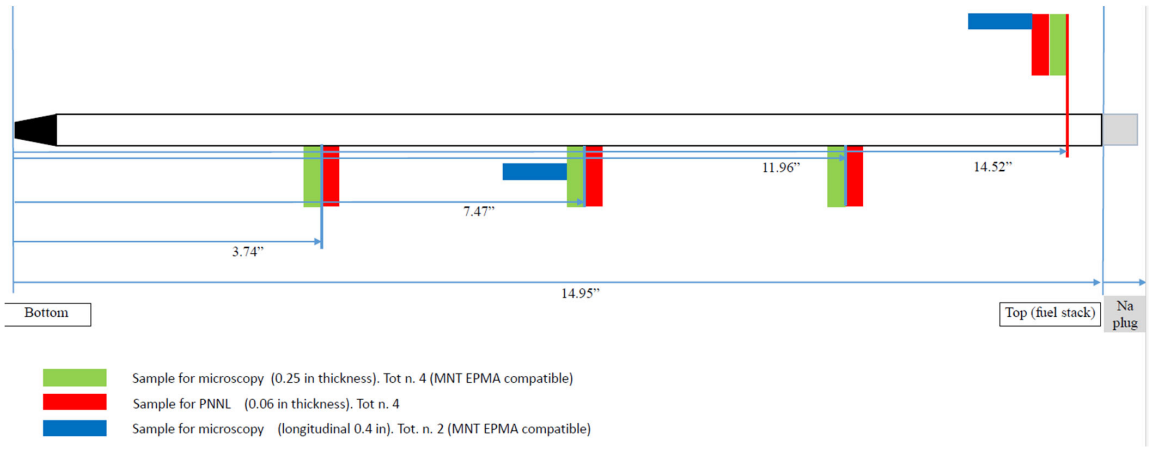

Figure 3. Cutting diagram for X430 T653.

3. Results

The pins discussed in the results below include DP45, DP61 from experiment X441A, DP20 from experiment X441, T653 from experiment X430B, A812, DP21, and DP29 from experiment X441A. These pins were chosen due to metallography being available for comparison, as well as the pins containing different smeared densities, irradiation lengths, outer diameters, fuel compositions, and linear heat rates. Average burnup results obtained from BISON simulations matched previous predictions, with peak burnup values exceeding previous predictions [1]. This is due to zirconium redistribution occurring within the U-Pu-Zr fuel, which creates a buildup of a uranium zone, leading to a higher fission rate density and larger peak burnup. Each of the seven pins listed in Table 5 are individually discussed and zirconium redistribution is compared between the BISON predictions and metallography. The discussion of the overall Zr redistribution modeling facilitates and addresses the Zr redistribution model fitment with metallography and how the model will impact future fuel performance result predictions.

Table 5. Metallography pin cutting locations.

Pin	Location (x/L)	Type of Cut
A812	0.3	Radial
	0.5	Radial
	0.65	Radial
	0.8	Radial
	0.95	Radial
DP20	0.5	Radial
DP21	0.5	Radial
	0.78	Radial
DP29	0.5	Radial
	0.78	Radial
DP45	0.5	Radial
	0.78	Radial
DP61	0.5	Radial
	0.78	Radial
	0.89	Radial
T653	0.25	Radial
	0.5	Radial
	0.5	Axial
	0.78	Radial
	0.97	Axial

3.1. DP45

Of the pins examined in this work, DP45 had the highest smear density, at 85%, and a moderate burnup of 8.87 at.%. The BISON simulation reached a slightly lower average burnup of 8.69%. Figure 4 displays the Zr mole fraction results comparing the BISON contour results and available metallography images. Examining Figure 4a closely, at 50% axial height, the three distinct zones in the metallography image are reflected by three distinct zones in the simulation results. The Zr-rich zone, indicated by red, aligns well with the central Zr-rich zone 1 seen in the metallography image and the Zr-depleted zone, blue, matches the thickness and radial position of zone 2 in the metallography. At 78% axial height, Figure 4b Zr-rich zone has migrated slightly beyond the central zone edge. At the outer edge of zone 1 and the start of zone 2, there seems to be a small section of moderate zirconium concentration, which is identified as zone 2 within A812 latter on within the results. However, the Zr-depleted zone is still the approximate thickness as the lighter Zr-depleted zone 2 seen in the image.

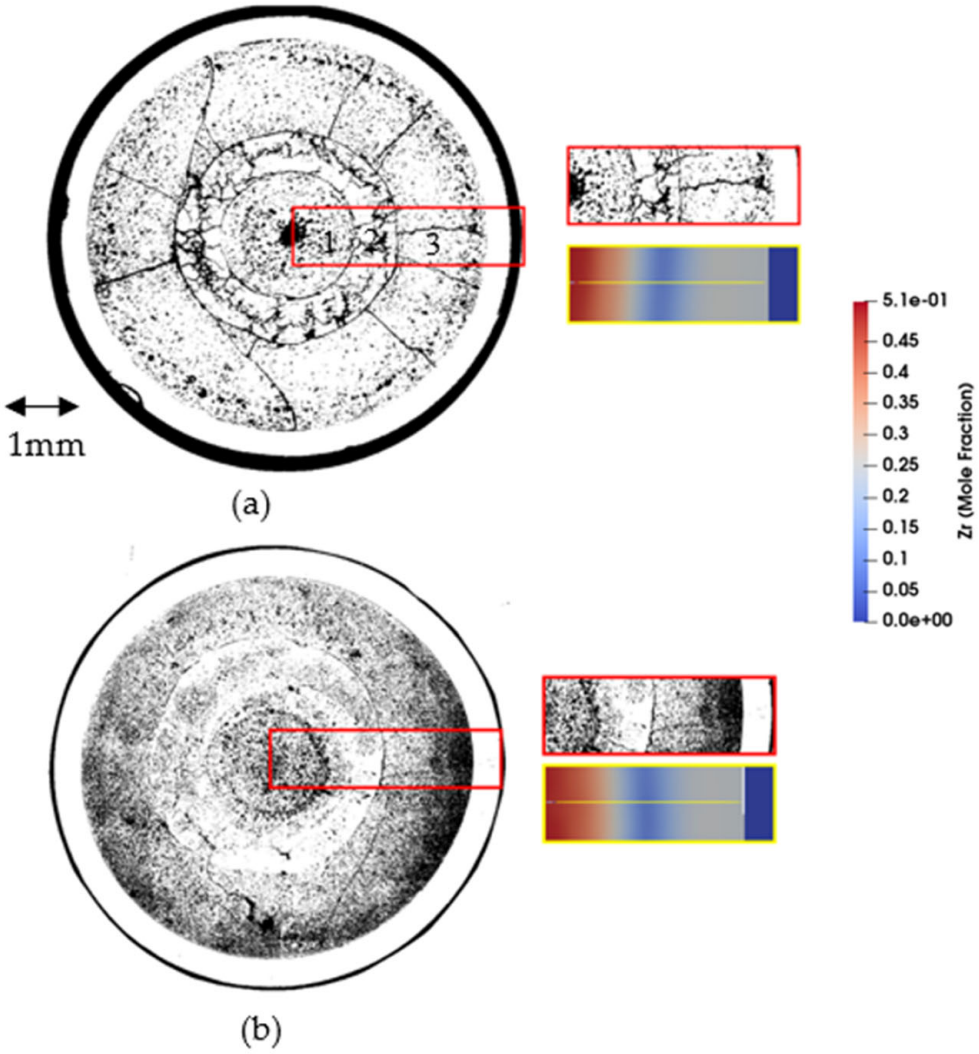

Figure 4. DP45 radial metallography image and BISON qualitative comparison. (**a**) X/L = 0.50 (**b**) X/L = 0.78 [8].

3.2. DP61

The second pin utilized to set the baseline model parameters was DP61. This pin had the lowest smeared density of the tested pins at 70%, with a higher burnup of 10.7 at.%. Figure 5 displays the comparison plots between the metallography images and BISON simulation results. The BISON results generally agree with the metallography images, although the lack of clear zone edges that were present in the DP45 images hinders the analysis slightly. The agreement between the Zr contour plots and the metallography degrades at higher axial heights as the Zr-depleted zone 2 is thicker and migrates further than the light-colored depleted zones in the images. Noticeable in all three results is the gap between the fuel pin and the cladding. The lack of contact is likely due to the low smeared density and the low terminating porosity used in the BISON simulations, however there is no gap apparent in the metallography images, indicating improvements to the fuel swelling eigenstrain model are needed in future work. The additional swelling needed will increase thermal resistance by having the sodium bond be displaced, causing the depletion zone to shift outward radially.

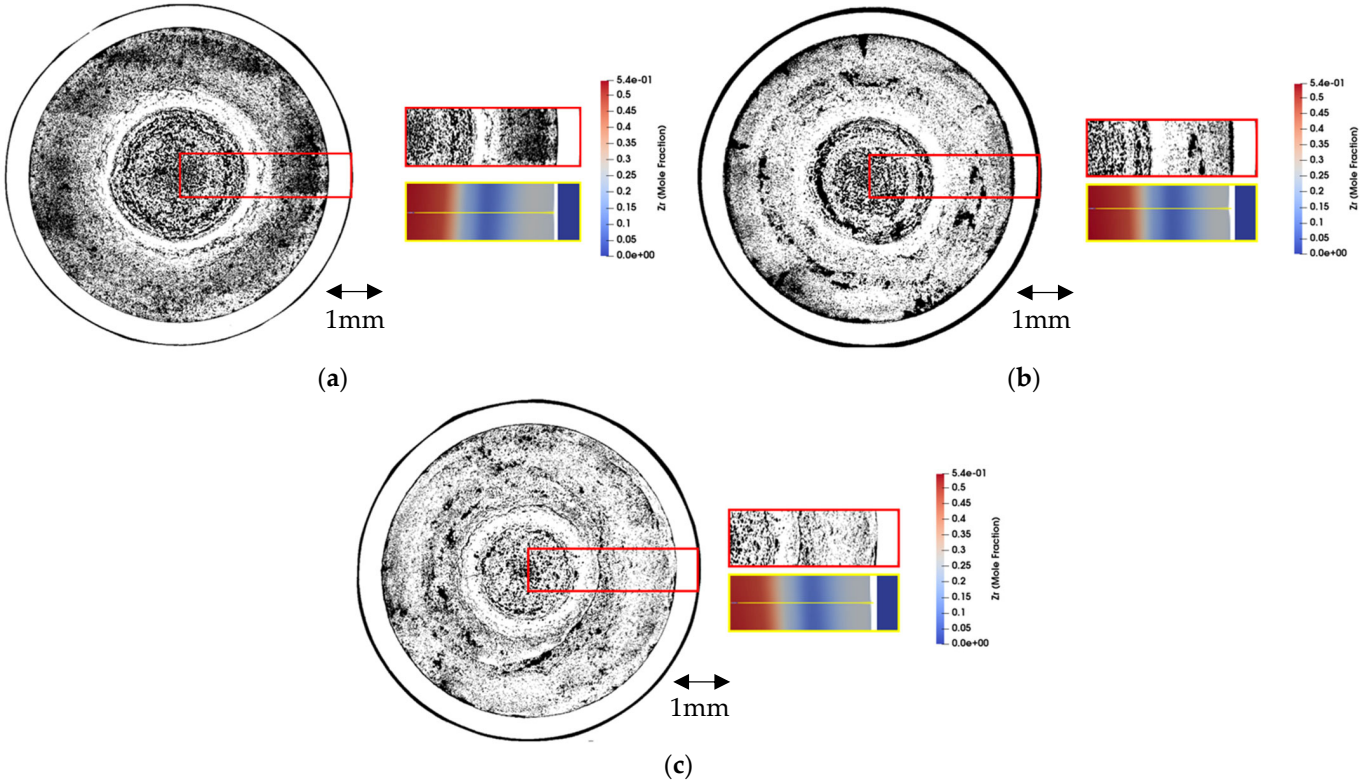

Figure 5. DP61 radial metallography image and BISON qualitative comparison. (**a**) X/L = 0.50 (**b**) X/L = 0.78 (**c**) X/L = 0.89 [7].

3.3. DP20

Of the EBR-II pins, simulated DP20 had the shortest irradiation history and an average burnup of 4.84 at.%. The BISON results, shown in Figure 6, agree with the metallography image, with the Zr-depleted zone 2 appearing in the same radial location as the Zr-depleted zone seen in the metallography image. The comparison could be slightly skewed due to the protrusion on the right side of the depleted zone within the metallography—the Zr-depleted zones within the DP45 and DP61 pins are fairly annular—the Zr-depleted zone 2 in the DP20 metallography is slightly misshapen. As mentioned within the DP61 results, complete closure of the fuel-cladding gap would increase thermal resistance, and the depletion zone radially shifting towards the cladding wall leading to a better comparison with the metallography.

3.4. T653

Pin T653 was the only analyzed pin from experiment X430B. Although from a different experiment, T653 reached an average burnup of 9.91 at.%, had a 75% smeared density, and was composed of U-19Pu-10Zr and HT9 cladding, which is in line with the other pins examined. Unfortunately, examining Figure 7, the BISON results lack clear zones and zone edges for 25% and 97% axial height, and 50% and 60% axial height, respectively. For the 25%, 50%, and 97% axial height metallography images, there appears to only be two zones present within the fuel pin when differentiating by color or clear edges, with three zones possible if defining by changes in porosity as well. If the 97% longitudinal image is taken to have three zones—the central Zr-rich zone 1, the thin Zr-depleted zone 2 filled with small black pores, and the outer moderately Zr-enriched zone 3 with relatively few pores—the BISON results faintly reflect the metallography. However, the BISON Zr-rich zone 1 does not migrate as considerably as the central Zr-rich zone 1. This suggests that either the boundary conditions at the top of the fuel surface need to be adjusted, or a variation within the EBR-II power history allowed for the change in fuel centerline temperature.

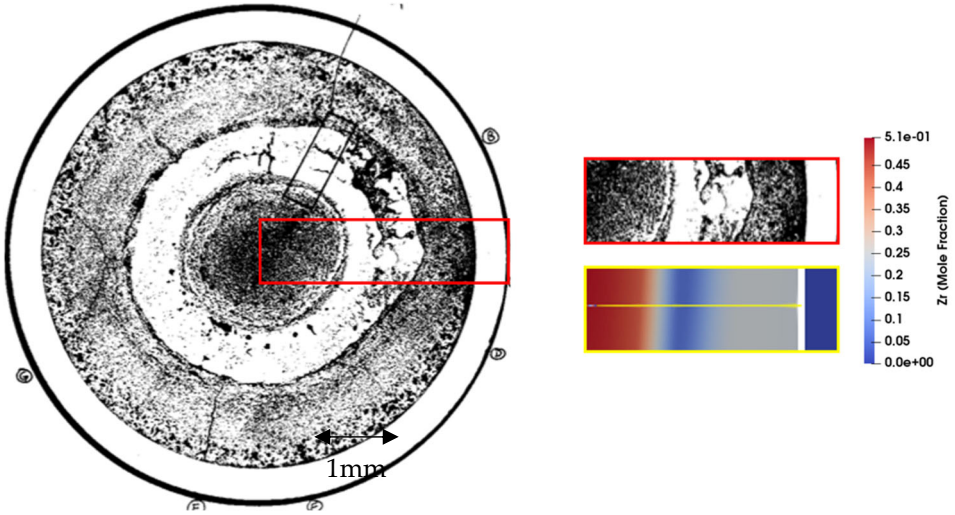

Figure 6. DP20 radial metallography image (X/L = 0.49) and BISON qualitative comparison [7].

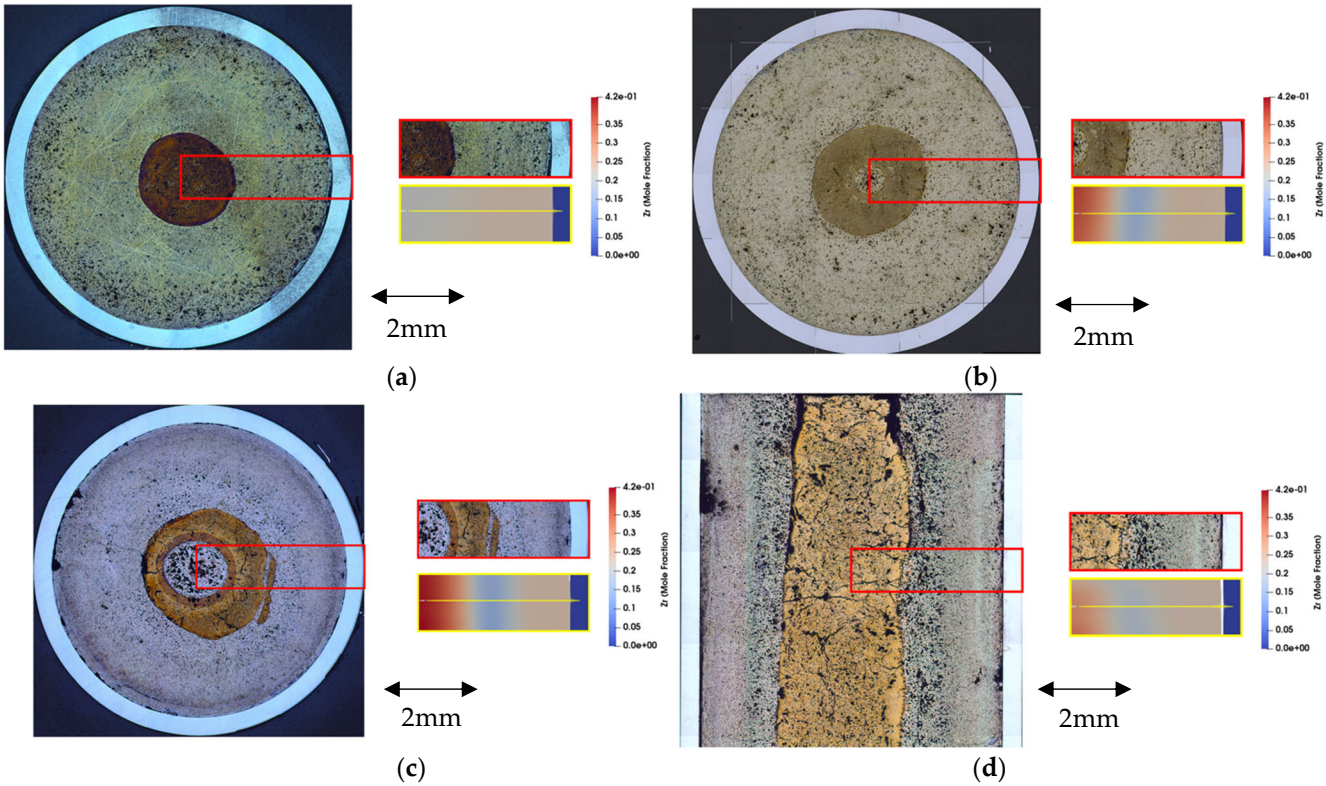

Figure 7. T653 radial and longitudinal metallography image and BISON qualitative comparison. (**a**) X/L = 0.25 (**b**) X/L = 0.50 (**c**) X/L = 0.60 (**d**) X/L = 0.97.

Shifting focus to the 60% axial height, where the zones in both the metallography image and the BISON results are well-defined, the central Zr-rich zone 1 migrates farther than is seen in the fuel pin. Moreover, the Zr-depleted zone 2 is thinner than the majority of the annular depleted zones seen in the image. Note within Figure 7c, the Zr-depleted zone is nonuniform, suggesting asymmetric cooling conditions. Additionally, the BISON simulation only reached a Zr mole fraction of 42%, which is significantly lower than the 51–60% mole fraction seen in the other analyzed pins. The causes behind these deviations from the relatively accurate results of the previous pins are due to differences in the linear power history and the thermal gradient, as well as the larger fuel diameter of this pin (0.572 cm) compared to the other fuel pins (0.432 cm). T653 exhibited a longer irradiation

time than the other fuel pins and did not experience the same power fraction as the pins in experiment X441 resulting in lower volumetric heat and lower temperatures.

3.5. A812

Fuel pin A812, seen in Figure 8, contains four zones within the pin which are in general agreement between the metallography and the BISON results for all five axial heights. At the 80% axial height location and higher on the fuel pin, the Zr-rich zone 1 migrates farther than the central Zr-rich zone 1 in the metallography images. In both the metallography and BISON results, there is a more prevalent zone 2 of moderate Zr-enrichment, in between the Zr-rich and Zr-depleted zones 1 and 3, than is not obviously seen in any of the other fuel pins. This is also the first time that this phenomenon has been captured within fuel performance simulations and compared to metallography. This moderately enriched zone matches well in the radial position and thickness for the first three axial height locations (X/L = 0.30, 0.50, 0.65), with an outward shift in radial position for the remaining two locations (X/L = 0.80, 0.95).

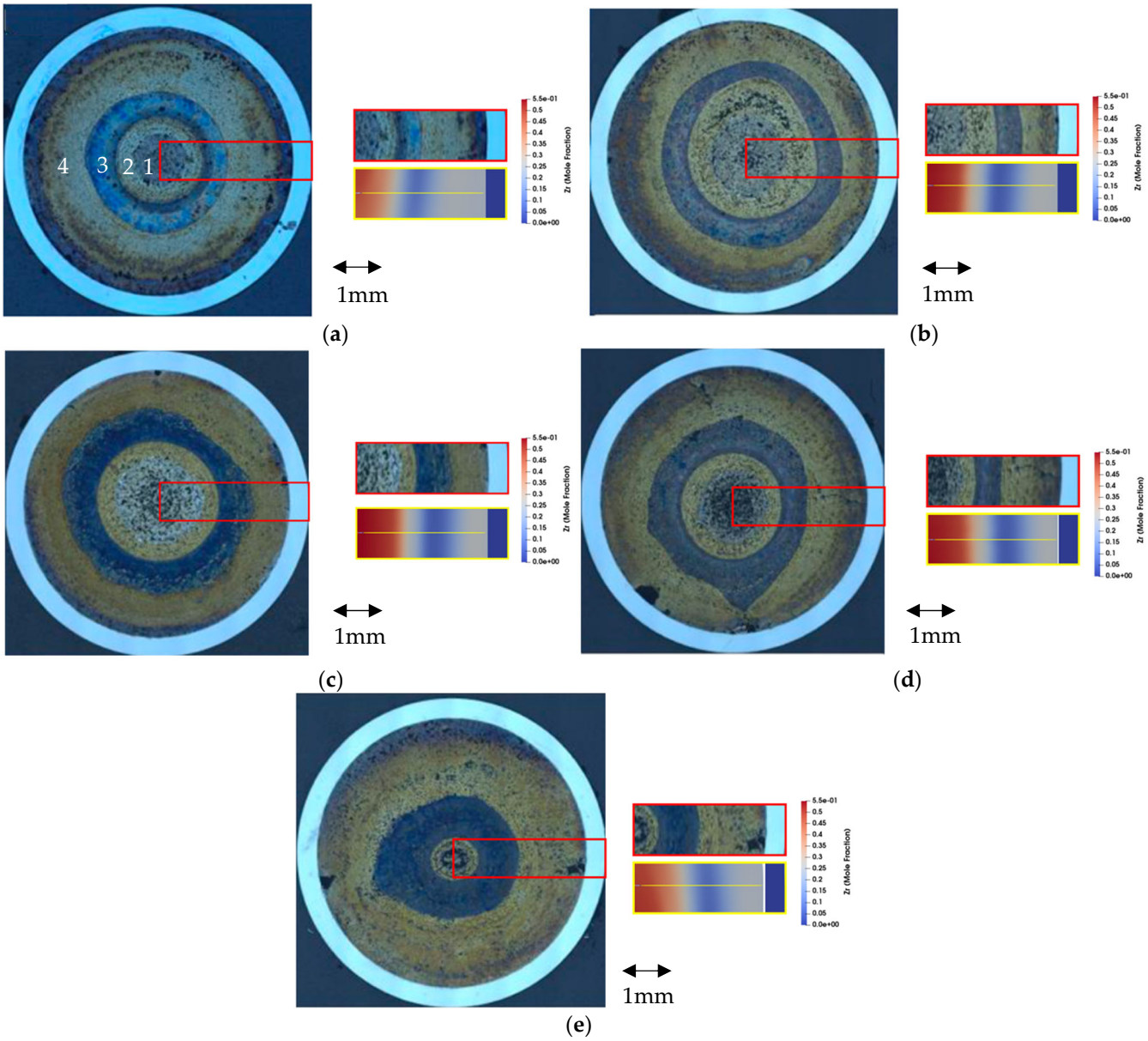

Figure 8. Radial metallography image and BISON qualitative comparison. (**a**) X/L = 0.30 (**b**) X/L = 0.50 (**c**) X/L = 0.65 (**d**) X/L = 0.80 (**e**) X/L = 0.95 [36,37].

3.6. DP21 and DP29

The remaining two fuel pins were experimentally analyzed between 1989 and 1991, along with DP61. Beginning with DP21, seen in Figure 9, there is good agreement between the metallography and BISON results for both axial heights. The Zr-rich zone is slightly thinner than the central Zr zone 1 in the images, however. This good agreement is likely due to the similarities in burnup, cladding, smeared density, and power history between DP21 and DP61.

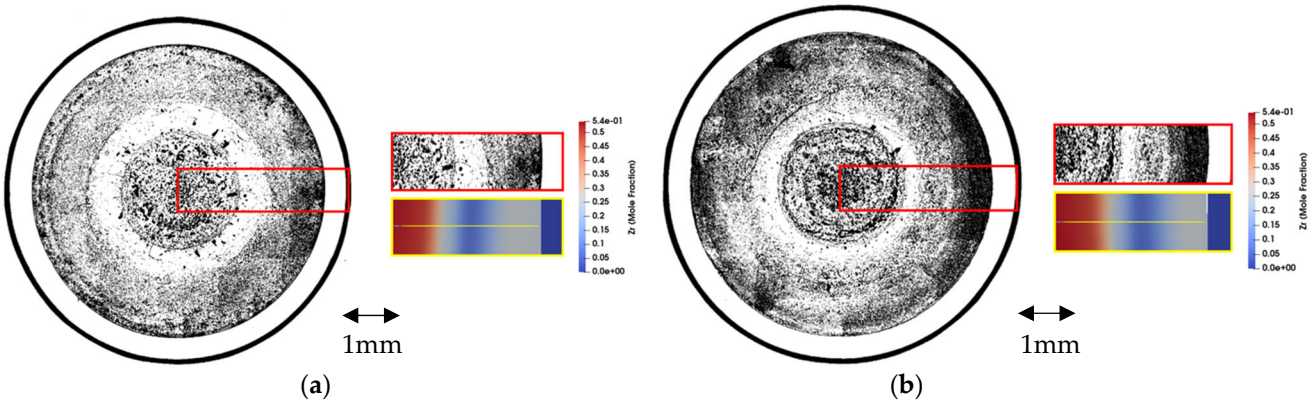

Figure 9. DP21 radial metallography image and BISON qualitative comparison. (**a**) X/L = 0.50 (**b**) X/L = 0.78 [7].

Conversely, DP29 began its irradiation life with 14 wt. % of Zr, compared to the 10 wt. % of the other pins. Nonetheless, the BISON results show good agreement with the metallography, seen in Figure 10. The Zr-depleted zones appear thicker than the thin white annulus of the Zr-depleted zones in the images.

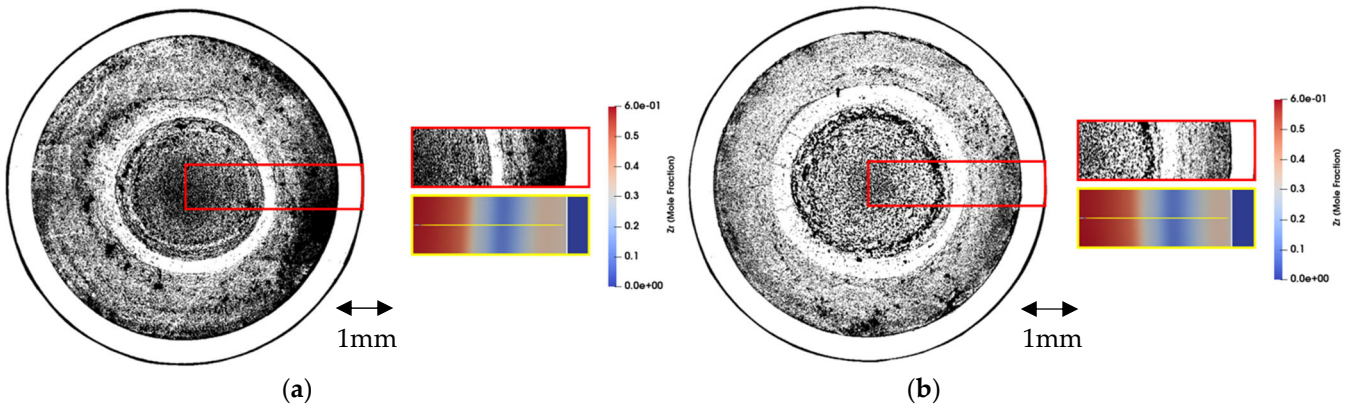

Figure 10. DP29 radial metallography image and BISON qualitative comparison. (**a**) X/L = 0.50 (**b**) X/L = 0.78 [7].

4. Discussion

Six of seven pins presented in this work were adequately able to replicate the zones shown within the metallography. This is a significant improvement within fuel performance modeling, as it shows that the majority of pins with varying irradiation parameters, power histories, geometry, and fuel and cladding compositions can successfully predict zirconium redistribution. These differences all affect the zoning and movement of zirconium and temperature distribution within the fuel matrix. In addition, being able to accurately predict the zirconium zones within the full matrix allows for better coupling within other fuel performance material models that are zirconium dependent, such as thermal conductivity, thermal creep, and modulus of elasticity.

In previous modeling works for metallic fuel zirconium redistribution, four zirconium zones have not been identified in fuel performance predictions, yet alone compared to

metallography. The reason for the four prominent zirconium zones within A812 compared to other pins within this work is due to the change in power history. The other six pins within this work operated at different LHGR's but were either mostly constant or gradually reduced in power. In the case of A812 and also within BISON predictions for DP16, there was a power reduction of 33%, allowing for beta phase of uranium to shift within the fuel matrix. The power history for A812 is shown in Figure 11 below. This allowed for zirconium to migrate from a three-zone regime that had already formed, into four distinct zones later in irradiation. This shows how important the irradiation parameters are and how a change in power history can affect the migration of zirconium and the number of zones, such as for the comparison performed for pin T653. This same effect could be noticeable in pins that also undergo an overpower transient, such as a loss of coolant accident, or after a core shuffle occurs within a reactor. Such testing within TREAT or ATR could provide more information on the diffusion scalars which determine the rate at which zirconium migrates apart from the thermal gradient within the fuel matrix.

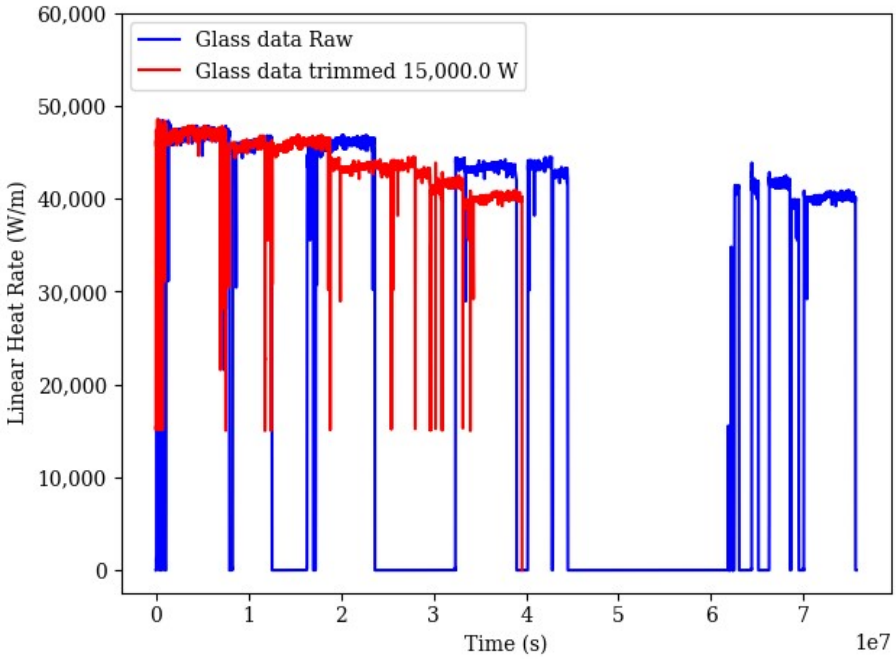

Figure 11. A812 power history.

Examining the zirconium redistribution predictions for the EBR-II pins, all the pins except for T653 showed relative agreement between the BISON simulations and the provided metallography images. The primary three zirconium zones are clearly present in each simulation result, with the A812 pin results displaying four zones as seen in the metallography. The simulation zones generally align with the edges of each zone in the images. However, at axial height locations X/L of 0.78 and higher, the BISON Zr-rich zones are slightly thicker than the central Zr-rich zones in the metallography. These high axial locations correspond to higher temperatures, which cause increased migration within the fuel. This suggests that there is additional cooling from the displaced sodium bond not considered on the top of the fuel surface during the simulations. This is confirmed in other works involving EBR-II experiment X501, as there is no zirconium-rich region at an axial height of X/L = 0.95 [38].

Contrary to the results for the other six fuel pins, the BISON simulations of pin T653 from experiment X430 do not match the metallography data well. At 50% and 60% axial height, the three Zr zones are present, although the metallography at 50% axial height only shows two clear zones and at 60% axial height the BISON results are shifted radially outward compared to the data. The three zones are indiscernible in the simulation results at the other axial heights of 25% and 97%. As discussed above, the lack of agreement

between the simulation results and metallography data is likely due to the differences in linear power history and coolant conditions between the baseline pins—DP45 and DP61 from experiment X441—and T653 from experiment X430 and the error associated within the power history from the GLASS data. All pins were run at the final model parameters detailed above in Table 4. To counteract this dependence, the model parameters should be baselined against numerous fuel pins with differing power histories, burnup rates and pin geometries. This would allow for the diffusion coefficients for the different phases of uranium to be optimized, similar to the work benchmarking pin T459 [2]. As more EPMA data becomes available for these legacy pins, the diffusion coefficient scalars can be optimized to better predict the zirconium concentrations within the fuel matrix.

Due to the success of BISON predictions matching the metallography well for the majority of pins, it is recommended that zirconium redistribution should be implemented into fuel performance modeling efforts for fuel pins that are expected to exhibit a uranium beta phase. This recommendation comes from the majority of fuel material properties being dependent on the zirconium concentration within the fuel matrix, which affects fuel performance metrics. With the recent implementation of pore collapse within BISON being creep dependent, the amount of zirconium within the fuel matrix will now affect the rate at which the fuel will swell and compress, which is the main contributor to cladding strain. Additions to the zirconium redistribution model could include a plutonium migration component, such that when plutonium migration is noticed, material properties that are plutonium-dependent may be accurately modeled.

5. Conclusions

Zirconium redistribution within metallic fuel pins is a vital step in validating the BISON code for use with future fuels. Seven fuel pins of differing dimensions and burnup rates were simulated and compared against PIE metallography images to improve the BISON model parameters. Past studies previously optimized various parameters, such as the phase transition temperatures and diffusion coefficient multipliers. However, the addition of new model parameters, such as partially-logged and logged porosity correction factor parameters, required the re-optimization of the combined model parameters. Pins DP45 and DP61 from experiment X441 were utilized as baselines to optimize these parameters. The pins were simulated with various parameter combinations of porosity correction factors, thermal conductivity models, phase transition temperatures, and diffusion coefficient multipliers. Numerous trials resulted in the selection of the final model combinations, which include the logged porosity correction factor, LANL thermal conductivity model, Galloway phase transition temperatures, and diffusion coefficient multipliers equal to 0.6.

Applying the final model parameters to the five other fuel pins further verified the selected parameters. Of the seven pins tested, six pins resulted in Zr migration that aligned well with the Zr zones seen in the metallography. The seventh pin, T653, produced results that did not accurately reflect the Zr redistribution in the metallography. The difference in results between T653 and the other pins indicated a possible dependence on the linear power history and thermal gradients of the fuel pins, since T653 is from experiment X430, while the other pins are from experiment X441.

Overall, the analyzed pins displayed good agreement between the BISON results and metallography data, verifying the applied model parameters and supporting the use of BISON for modeling metallic fuels. Future work should be conducted to further optimize the applied model parameters. In particular, data should be collected from the physical specimens, including EPMA and metallography data at low axial heights, for improved comparison against the model results. Additional EPMA data will provide numerical data for a quantitative comparison alongside the qualitative comparison results of this work. An effort should be made to utilize fuel pins from different experiments, with a range of linear power histories and burnup values in order to optimize the model parameters for general use.

Author Contributions: Conceptualization, K.M.P., S.C., L.C., A.A. and D.P.; methodology, K.M.P. and S.C.; software, K.M.P. and S.C.; validation, K.M.P.; formal analysis, K.M.P. and S.C.; investigation, K.M.P., S.C. and L.C.; resources, K.M.P., L.C., A.A. and D.P.; data curation, K.M.P., S.C. and L.C.; writing—original draft preparation, K.M.P. and S.C.; writing—review and editing, K.M.P.; visualization, K.M.P. and S.C.; supervision, K.M.P., L.C. and D.P.; project administration, K.M.P., L.C. and D.P.; funding acquisition, D.P. All authors have read and agreed to the published version of the manuscript.

Funding: This work was funded by the Office of Nuclear Energy under DOE Idaho Operations Office Contract DE-AC07-051D14517 as part of a Nuclear Science User Facilities experiment.

Data Availability Statement: The raw/processed data required to reproduce these findings cannot be shared at this time due to export control.

Acknowledgments: I would like to acknowledge Adam X. Zabriskie and Matthew Kerr for providing review input, knowledge, and experimental data. For A812 metallography: This work was supported by the U.S. Department of Energy, Office of Nuclear Energy under DOE Idaho Operations Office Contract DE-AC07-051D14517 as part of a Nuclear Science User Facilities experiment.

Conflicts of Interest: The authors declare no conflict of interest.

Abbreviations

ANL	Argonne National Laboratory
CDF	Cumulative Damage Fraction
EBR-II	Experimental Breeder Reactor II
EDS	Energy Dispersive X-ray Spectroscopy
EPMA	Electron Probe Microanalyses
FCCI	Fuel Cladding Chemical Interaction
FFTF	Fast Flux Test Facility
FGR	Fission Gas Release
FIPD	Fuels Irradiation and Physics Database
GLASS	Germanium-Lithium Argon Scanning System
GUI	Graphics User Interface
IMIS	IFR Materials Information System
INL	Idaho National Laboratory
LHGR	Linear Heat Generation Rate
LWR	Light Water Reactor
MOOSE	Multiphysics Object Orientated Simulation Environment
PIE	Post Irradiation Examination
SEM	Secondary Electron Microscopy
SFR	Sodium-cooled Fast Reactor
SMR	Small Modular Reactor
VTR	Versatile Test Reactor

References

1. Paaren, K.M.; Gale, M.; Kerr, M.J.; Medvedev, P.; Porter, D. Initial demonstration of automated fuel performance modeling with 1977 EBR-II metallic fuel pins using BISON code with FIPD and IMIS databases. *Nucl. Eng. Des.* **2021**, *382*, 111393. [CrossRef]
2. Galloway, J.; Unal, C.; Carlson, N.; Porter, D.; Hayes, S. Modeling constituent redistribution in U–Pu–Zr metallic fuel using the advanced fuel performance code BISON. *Nucl. Eng. Des.* **2015**, *286*, 1–17. [CrossRef]
3. Harp, J.M.; Porter, D.L.; Miller, B.D.; Trowbridge, T.L.; Carmack, W.J. Scanning electron microscopy examination of a Fast Flux Test Facility irradiated U-10Zr fuel cross section clad with HT-9. *J. Nucl. Mater.* **2017**, *494*, 227–239. [CrossRef]

4. Porter, D.L.; Lahm, C.E.; Pahl, R.G. Fuel constituent redistribution during the early stages of U-Pu-Zr irradiation. *Metall. Trans. A* **1990**, *21*, 1871–1876. [CrossRef]
5. Ohta, H.; Ogata, T.; Papaioannou, D.; Rondinell, V.V.; Masson, M.; Paul, J.-L. Irradiation of Minor Actinide–Bearing Uranium-Plutonium-Zirconium Alloys up to ~2.5 at.%, ~7 at.%, and ~10 at.% Burnups. *Nucl. Technol.* **2015**, *190*, 36–51. [CrossRef]
6. Hales, J.; Novascone, S.; Spencer, B.; Williamson, R.; Pastore, G.; Perez, D. Verification of the BISON fuel performance code. *Ann. Nucl. Energy* **2014**, *71*, 81–90. [CrossRef]
7. Galloway, J.D.; Unal, C.; Matthews, C. *Constituent Redistribution in U-Zr Metallic Fuel Using the Advanced Fuel Performance Code BISON*; Los Alamos National Laboratory (LANL): Los Alamos, NM, USA, 2016. [CrossRef]
8. Matthews, C.; Galloway, J.; Unal, C.; Novascone, S.; Williamson, R. *BISON for Metallic Fuels Modelling*; International Atomic Energy Agency (IAEA): Vienna, Austria, 2017.
9. Matthews, C.; Unal, C.; Galloway, J.; Keiser, D.D., Jr.; Hayes, S.L. Fuel-Cladding Chemical Interaction in U-Pu-Zr Metallic Fuels: A Critical Review. *Nucl. Technol.* **2017**, *198*, 231–259. [CrossRef]
10. Galloway, J.D. *Fully-Coupled Metallic Fuel Performance Simulations Using BISON*; Los Alamos National Laboratory (LANL): Los Alamos, NM, USA, 2015.
11. Yacout, A.M.; Oaks, A.; Mohamed, W.; Mo, K. *FIPD: EBR-II Fuels Irradiation & Physics Database*; Argonne National Laboratory (ANL): Argonne, IL, USA, 2017. [CrossRef]
12. Porter, D.; Mariani, R.D. *Archiving EBR-II Metallic Fuel Test Data Using NDMAS to Accelerate Fast Reactor Fuel Qualification*; Idaho National Laboratory (INL): Idaho Falls, ID, USA, 2019.
13. Paaren, K.M.; Lybeck, N.; Mo, K.; Medvedev, P.G.; Porter, D.L. Cladding Profilometry Analysis of EBR-II metallic fuel pins with HT9, D9, and SS316 cladding. *Energies* **2021**, *14*, 515. [CrossRef]
14. Paaren, K.M.; Black, A.; Lybeck, N.; Mo, K.; Spencer, B.W.; Medvedev, P.; Porter, D. BISON Fuel Performance Modeling Optimization for Experiment X447 and X447A Using Axial Swelling and Cladding Strain Measurements. *Nucl. Eng. Des.* **2022**, *394*, 111812. [CrossRef]
15. Kim, Y.S.; Hayes, S.L.; Hofman, G.L.; Yacout, A.M. Modeling of constituent redistribution in U–Pu–Zr metallic fuel. *J. Nucl. Mater.* **2006**, *359*, 17–28. [CrossRef]
16. Billone, M.C.; Liu, Y.Y.; Gruber, E.E.; Hughes, T.H.; Kramer, J.M. Status of Fuel Element Modeling Codes for Metallic Fuels. In Proceedings of the International Conference on Reliable Fuels for Liquid Metal Reactors, Tuson, AZ, USA, 7–11 September 1968.
17. Savage, H. The heat content and specific heat of some metallic fast-reactor fuels containing plutonium. *J. Nucl. Mater.* **1968**, *25*, 249–259. [CrossRef]
18. Hofman, G.L.; Billone, M.C.; Koenig, J.F.; Kramer, J.M. *Metallic Fuels Handbook*; Argonne National Laboratory (ANL): Argonne, IL, USA, 2019.
19. Banerjee, A.; Raju, S.; Divakar, R.; Mohandas, E. High Temperature Heat Capacity of Alloy D9 Using Drop Calorimetry Based Enthalpy Increment Measurements. *Int. J. Thermophys.* **2007**, *28*, 97–108. [CrossRef]
20. Leibowitz, L.; Blomquist, R.A. Thermal conductivity and thermal expansion of stainless steels D9 and HT9. *Int. J. Thermophys.* **1988**, *9*, 873–883. [CrossRef]
21. Yamanouchi, N.; Tamura, M.; Hayakawa, H.; Kondo, T. Accumulation of engineering data for practical use of reduced activation ferritic steel: 8%Cr-2%W-0.2%V-0.04%Ta-Fe. *J. Nucl. Mater.* **1992**, *191–194*, 822–826. [CrossRef]
22. Mills, K.C. *Recommended Values of Thermophysical Properties for Selected Commercial Alloys*; Woodhead Publishing: Cambridge, UK, 2002.
23. Bauer, T. In-Pile Measurement of the Thermal Conductivity of Irradiated Metallic Fuel. *Nucl. Technol.* **1995**, *110*, 407–421. [CrossRef]
24. Olander, D.R. *Fundamental Aspects of Nuclear Reactor Fuel Elements*; Technical Information Center, Energy Research and Development Administration: Oak Ridge, TN, USA, 1976.
25. Hales, J.D.; Gamble, K.A.; Spencer, B.W.; Novascone, S.R.; Pastore, G.; Liu, W.; Stafford, D.S.; Williamson, R.L.; Perez, D.M.; Gardner, R.J. *BISON Users Manual-BISON Release 1.2*; Idaho National Laboratory: Idaho Falls, ID, USA, 2015.
26. Los Alamos National Laboratory. *AFCI Materials Handbook, Materials Data for Particle Accelerator Applications, Chapter 18-Design Properties of HT9 and Russian Ferritic/Martensitic Steels, Rev 6*; Los Alamos National Laboratory (LANL): Los Alamos, NM, USA, 2014.
27. Garner, F.; Porter, D. Irradiation creep and swelling of AISI 316 to exposures of 130 dpa at 385–400 °C. *J. Nucl. Mater.* **1988**, *155–157*, 1006–1013. [CrossRef]
28. GeelHood, K.J.; Porter, I.E. Modeling and Assessment of EBR-II Fuel with the US NRC's Fast Fuel Performance Code. In Proceedings of Top Fuel 2018, Prague, Czech Republic, 30 September–4 October 2018; p. 12.
29. American Society of Mechanical Engineers. *ASME Boiler and Pressure Vessel Code*; American Society of Mechanical Engineers: New York, NY, USA, 2016.
30. Ogata, T.; Takeshi, Y. Development and Validation of ALFUS: An Irradiation Behavior Analysis code for Metallic Fast Reactor Fuels. *Nucl. Technol.* **1999**, *128*, 113–124. [CrossRef]
31. Karahan, A.; Buongiorno, J. Modeling of thermo-mechanical and irradiation behavior of mixed oxide fuel for sodium fast reactors. *J. Nucl. Mater.* **2010**, *396*, 272–282. [CrossRef]
32. Hofman, G.L.; Walters, L.C.; Bauer, T.H. Metallic Fast Reactor Fuels. *Prog. Nucl. Energy* **1997**, *31*, 83–110. [CrossRef]

33. Pitner, A.L.; Gneiting, B.C.; Bard, F.E. Irradiation Performance of Fast Flux Test Facility Drivers Using D9 Alloy. *Nucl. Technol.* **1995**, *112*, 194–203. [CrossRef]
34. Briggs, L.; Chang, Y.; Hill, D.; Ahrens, J.; Billone, M.; Crawford, D.; Filewicz, E.; Finck, P.; Fujita, E.; Grimm, K.; et al. *Safety Analysis and Technical Basis for Establing an Interim Burnup Limit for Mark-V and Mark-VA Fuel Subassemblies in EBR-II*; Argonne National Laboratory (ANL): Argonne, IL, USA, 1995. [CrossRef]
35. Karahan, A.; Buongiorno, J. A new code for predicting the thermo-mechanical and irradiation behavior of metallic fuels in sodium fast reactors. *J. Nucl. Mater.* **2010**, *396*, 283–293. [CrossRef]
36. Capriotti, L.; Harp, J. *Status PIE Report on Legacy EBR-II and FFTF Metallic Fuel Experiments-INL/EXT-19-55847*; Idaho National Laboratory (INL): Idaho Falls, ID, USA, 2019.
37. Rahn, T.; Capriotti, L.; Di Lemma, F.; Trowbridge, T.L.; Harp, J.M.; Aitkaliyeva, A. Investigation of constituent redistribution in U-Pu-Zr fuels and its dependence on varying Zr content. *J. Nucl. Mater.* **2021**, *557*, 153301. [CrossRef]
38. Capriotti, L.; Harp, J.M. Characterization of a minor actinides bearing metallic fuel pin irradiated in EBR-II. *J. Nucl. Mater.* **2020**, *539*, 152279. [CrossRef]